NASA TECHNICAL NOTE

NASA TN D-2879

DESIGN AND OVERALL PERFORMANCE OF A TWO-STAGE AXIAL-FLOW PUMP WITH A TANDEM-ROW INLET STAGE

by Donald M. Sandercock and James E. Crouse

Lewis Research Center

Cleveland, Ohio

NATIONAL AERONAUTICS AND SPACE ADMINISTRATION • WASHINGTON, D. C. • JUNE 1965

NASA TN D-2879

DESIGN AND OVERALL PERFORMANCE OF A TWO-STAGE AXIAL-FLOW PUMP WITH A TANDEM-ROW INLET STAGE

By Donald M. Sandercock and James E. Crouse

Lewis Research Center
Cleveland, Ohio

NATIONAL AERONAUTICS AND SPACE ADMINISTRATION

For sale by the Clearinghouse for Federal Scientific and Technical Information
Springfield, Virginia 22151 – Price $2.00

DESIGN AND OVERALL PERFORMANCE OF A TWO-STAGE AXIAL-FLOW PUMP WITH A TANDEM-ROW INLET STAGE

by Donald M. Sandercock and James E. Crouse

Lewis Research Center

SUMMARY

The inlet stage group for a high suction specific speed, multistage axial-flow pump was designed and tested in water. Inlet flow vector diagrams were optimized for suction specific speed at a suction specific speed of 30 000. The first stage had a tandem arrangement of a cambered, tapered inducer and a transition rotor that adds enough head to keep the following highly loaded stages free of cavitation at design flow. The first-stage stator set up flow conditions suitable for the highly loaded rotor.

Under noncavitating conditions, the pump performance at design flow was below the anticipated head and efficiency because the transition and second-stage rotors failed to achieve anticipated energy addition and efficiency. As the flow coefficient was reduced below 0. 9, the pump developed regions of reverse flow. The characteristic had little drop in head rise in the stall range. The off-design blade row characteristics showed major redistributions of work between rotors.

At design flow and a suction specific speed of 27 000 in water, the pump head rise had begun to fall from the noncavitating values.

Author

INTRODUCTION

The primary function of inlet stages of a high suction specific speed multistage axial-flow pump is to accept cavitation but continue to produce sufficient pressure to suppress cavity formation and prevent its occurrence in main pressure producing portions of the pump. The inlet stage experiences significant amounts of two-phase flow; its first blade row, or inducer, characteristically includes high blade stagger angles (as measured from the axial direction), a small number of blades, large solidities, low hub-tip radius ratios, and low blade loading. In contrast, the design of the high pressure producing stages with single-phase flow employ lower blade stagger angles (50° to 70°), lower

solidities, larger numbers of blades, higher hub-tip radius ratios, and limiting values of blade loading. These two types of stages are linked by means of one or more transition stages. Minimum pump weight will be realized when the number of transition stages is minimized.

In this study, the usual inducer and a transition stage have been combined into a single stage composed of a tandem arrangement of two rotating blade rows followed by a single stator row. Thus the inducer rotor, the transition rotor, and the stator row comprise the first stage. The test pump configuration is completed by the addition of a rotor of the type used in the high pressure producing portion of a multistage axial-flow pump. The first rotating blade row is typical of inducers including a low level of loading, a low hub-tip radius ratio, and several long-chord blades. The tandem-mounted transition rotor utilizes conventional blade shapes and chord lengths together with an increased level of loading. Such an arrangement would eliminate one stator row with the sacrifice of the cavitation reduction effects of the stator static pressure rise; alternately, as compared with the rear portion of a single extended chord rotor, the transition rotor starts its loading with clean surface boundary layers.

This report presents design procedures and overall performance of this multistage pump under noncavitating and cavitating flow conditions. The variation of head rise across the midspan of each blade row as flow is reduced through the stall region to shutoff is also presented.

PUMP DESIGN

Overall Design Considerations

At the initiation of this design, it was anticipated that the pump evolved would be operated in both water and liquid hydrogen. Consequently, operation in both fluids and the capabilities of water and liquid hydrogen test facilities were considered in selecting design parameters.

It was desired to obtain a suction specific speed of 30 000 with this pump. From optimization procedures similar to those outlined in reference 1, a suction specific speed of 30 000, a hub-tip radius ratio of 0.4, and the assumption of no inlet whirl combines to give an optimum relation between the axial velocity and blade speed of

$$\frac{V_z}{U} = 0.108 \tag{1}$$

(Symbols are defined in appendix A.) If equation (1) is applied at the blade tip location,

this relation becomes, by definition, the ideal inlet flow coefficient, or

$$\frac{V_{z,1}}{U_{t,1}} = \varphi_{1,i} = 0.108$$

The selection of an outer diameter of 6.50 inches was based primarily on considerations of liquid hydrogen test facility capability and acceptable length of operating time in liquid hydrogen. Flow rates were calculated by combining the design flow coefficient and the hub-tip radius ratio of 0.4 with a number of typical operating speeds in liquid hydrogen.

It is desirable from both cavitation and blade loading considerations that the flow coefficient increase (area decrease) when progressing from inlet stages with high suction specific speeds and low blade loading to latter stages with lower suction specific speeds and higher blade loading. In this design the average flow coefficient is increased by a factor of two from the inlet of the first rotating blade row (inducer) to the inlet of the second-stage rotor. Half of this increase is accomplished across the inducer and the remaining across the transition rotor of the first stage. No change in average flow coefficient was used across the second-stage rotor.

A preliminary sketch of the flow path contour based on the aforementioned area variation, a constant tip diameter, typical axial depths for each blade row, and sufficient spacing between blade rows to permit survey instrumentation to be used was constructed. The sketch showed a severe inducer hub curvature and a hub-tip radius ratio of 0.761 with a blade height of 0.776 inch for the second-stage rotor. In order to alleviate the hub curvature (and its affects on radial equilibrium requirements) and to improve the blade height of the second and any succeeding stages, the outer wall casing was tapered linearly across the inducer row to 0.95 of the inlet diameter (from 6.500 to 6.175 in.). For the same flow coefficient variation across the first stage, the hub-tip radius ratio of the second-stage rotor becomes 0.720 with a blade height of 0.865 inches. A sketch of

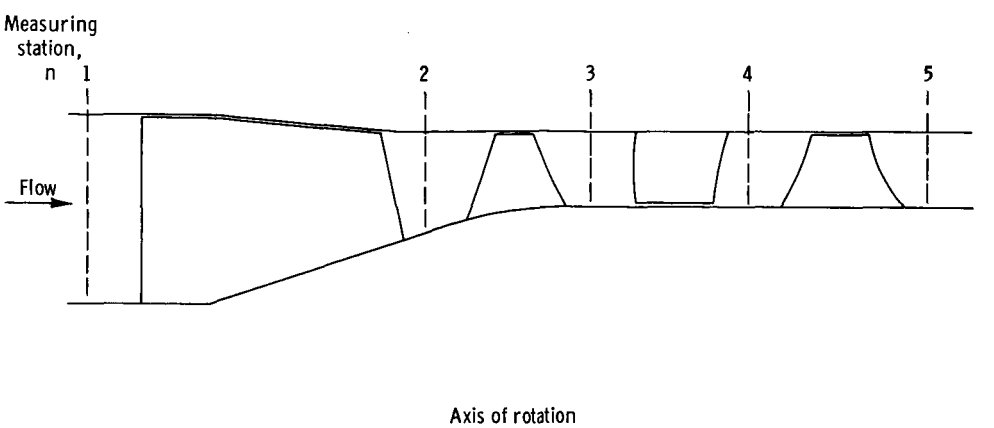

Figure 1. - Meridional view of axial-flow pump.

this flow passage showing axial location of measuring stations is presented in figure 1.

In this design, the head rise coefficient of each rotating blade row was constant from hub to tip. Radially constant total pressure tends to minimize mixing losses and reduce radial gradients of axial velocity thus easing matching problems with succeeding blade rows. Additional guide lines used to select approximate design levels of blade loading or head rise coefficient, radial distributions of loss coefficient, and type of velocity diagram in the various blade rows were as follows:

(1) A design head rise coefficient of approximately 0.120 was selected for the inducer. This value is consistent with the level of performance generally obtained from inducers with good cavitation performance. This head rise coefficient would provide a cavitation number (see eq. (B12a)) of approximately 0.3 at the inlet to the transition rotor tip element.

(2) Blade loading across the transition rotor was limited to a blade diffusion factor of approximately 0.4 in the blade tip region and 0.6 at all other radial locations. Velocity diagrams at the transition rotor outlet were calculated from the inducer inlet velocity diagrams and a design head rise coefficient and a radial distribution of loss coefficient assumed to occur across the two rotating blade rows.

(3) Velocity diagrams for the second-stage rotor utilized some inlet whirl at all radial locations. This reduces the cavitation number requirements at the rotor inlet and tends to equalize the portion of overall stage diffusion accomplished across the rotor and stator blade rows. A rather high design blade diffusion factor of approximately 0.55 at the blade tip was selected.

Having determined pump geometry and a preliminary value of overall head rise coefficient, a pump rotational speed of 5415 rpm for operation in water was selected. Principal factors affecting this selection were the limiting pressures of the collector downstream of the pump and the need for obtaining as high an inlet pressure corresponding to the 30 000 suction specific speed operating condition as possible.

Detailed Blade-Row Design

The pump detailed design approach is based on the assumptions of blade element flow and axial symmetry. The blade element approach assumes that flow in the circumferential plane may be described by considering the flow about blade profiles formed by the intersection of a flow surface of revolution with pump blading. Axial symmetry assumes that the flow conditions in the circumferential, or blade-to-blade, plane can be represented by an average value. Equations describing the radial variations of these values are written from continuity, energy addition, and pressure equilibrium from hub to tip.

In this design, the blade elements were assumed to lie on conical surfaces intersecting the blade inlet and outlet computational planes at radii enclosing equal portions of weight flow. Simple radial equilibrium (refs. 2 and 3), as defined by

$$\frac{\partial h}{\partial r} = \frac{V_\theta^2}{gr} \tag{2}$$

was applied in all design computations. The form equation (2) takes when used in a design application is given in appendix B together with other design equations.

Velocity diagrams were computed at the inlet and outlet of each blade row at 11 radial locations that divided the total flow into 10 equal portions. The large number of flow surfaces used reflects the convenience of being able to program the design equations for solution on a high-speed computing machine rather than an accuracy requirement. Design parameter together with velocity diagram calculations based on a pump inlet tip speed of 153.5 feet per second are tabulated in tables I (p. 6) and II (p. 7) for a selected number of blade elements.

At the first rotor inlet the velocity diagrams are based on the assumptions of (1) no inlet whirl ($V_{\theta,1} = 0$) and (2) a radially constant inlet flow coefficient.

The radial distribution of inducer outlet velocity diagrams was calculated from the equations listed in appendix B. Known inputs to the equations, include flow rate, passage hub and tip radii, inlet velocity diagrams, and selected radial distributions of head rise and loss coefficient. The latter were selected primarily on the basis of loss distributions measured during operation of a low hub-tip radius ratio rotor in water.

From the inducer blade trailing edge (inducer outlet computational plane) to the transition rotor blade leading edge (transition rotor inlet computational plane), a significant change in flow area occurs due to hub slope and the relatively large axial clearance space. In order to obtain more accurate inlet flow conditions to the transition rotor, the inducer outlet velocity diagrams were corrected by accounting for change in area and conservation of angular momentum with change of radius. The velocity diagrams at the transition rotor outlet were computed from the inducer inlet diagrams, the desired head rise to be produced by the inducer and transition rotors, and an assumed radial distribution of loss coefficient that would occur in the flow across the two rotating rows. This overall loss coefficient distribution was calculated from the loss coefficient distributions assumed for the inducer and transition rotors individually. The latter were chosen from experience with rotors operating in water (e.g., ref. 4).

The first-stage stator must accept the outlet flow from the transition rotor and turn it to the direction required by inlet velocity diagrams of the second-stage rotor design. Hence, the stator design is dependent upon the designs of both the preceding and succeeding rotors.

The conditions chosen for the second-stage rotor design were as follows:

TABLE I. - DESIGN VELOCITY DIAGRAMS

Axial station	Streamline number	Radius, r, in.	Absolute axial velocity, V_z, ft/sec	Absolute velocity, V, ft/sec	Flow angle, β, deg	Relative absolute velocity, V', ft/sec	Relative flow angle, β', deg	Rotor tangential velocity, U, ft/sec
1	0	3.250	16.5	16.5	0	154.4	83.9	153.5
	2	2.964	↓	↓	↓	141.0	83.3	140.0
	4	2.647				126.2	82.5	125.1
	6	2.287				109.3	81.4	108.1
	8	1.859				89.4	79.4	87.8
	10	1.296	↓	↓	↓	63.4	75.0	61.2
2a	0	3.087	19.0	35.2	57.4	117.7	80.7	145.8
	2	2.844	23.8	37.1	50.1	108.4	77.3	134.3
	4	2.626	26.6	38.8	46.7	99.4	74.5	124.0
	6	2.411	28.3	40.6	45.8	89.4	71.6	113.9
	8	2.189	29.8	42.6	45.7	78.7	67.8	103.4
	10	1.954	31.3	45.2	46.3	67.3	62.3	92.3
2b	0	3.087	23.8	38.0	51.3	118.6	78.5	145.8
	2	2.890	27.7	39.4	45.4	111.9	75.7	136.5
	4	2.705	30.0	40.7	42.4	104.8	73.3	127.8
	6	2.520	31.4	42.0	41.5	96.5	71.0	119.1
	8	2.329	32.6	43.4	41.3	87.7	68.2	110.1
	10	2.130	33.8	45.2	41.6	78.3	64.4	100.7
3	0	3.087	19.6	69.4	73.6	81.7	76.1	145.8
	2	2.864	30.3	73.1	65.5	75.2	66.3	135.3
	4	2.700	36.4	76.6	61.6	70.3	58.8	127.5
	6	2.550	39.8	80.0	60.2	64.8	52.1	120.5
	8	2.404	42.5	83.6	59.5	59.4	44.3	113.6
	10	2.258	44.9	87.6	59.2	54.8	35.0	106.7
4	0	3.087	35.9	42.2	31.8	128.7	73.8	145.8
	2	2.950	34.2	42.8	37.0	114.8	72.7	135.3
	4	2.800	33.0	43.7	40.9	104.3	71.5	127.5
	6	2.635	32.2	45.0	44.2	94.8	70.1	120.5
	8	2.456	31.7	46.6	47.2	85.5	68.3	113.6
	10	2.258	31.7	48.9	49.5	76.5	65.5	106.7
5	0	3.087	33.1	85.0	67.1	75.2	63.9	145.8
	2	2.940	↓	88.6	68.1	65.7	59.8	138.9
	4	2.785		92.9	69.1	55.7	53.6	131.6
	6	2.622		98.0	70.3	45.8	43.8	123.9
	8	2.447		104.2	71.5	37.1	27.0	115.6
	10	2.258	↓	112.0	72.8	33.1	-.5	106.7

TABLE II. - BLADE ELEMENT DESIGN PARAMETERS

Blade row	Streamline number	Radius, r, in.		Entrance flow coefficient, φ_e [U_t = 153.5]	Rotor head rise coefficient, ψ [U_t = 145.8]	Rotor efficiency, η	Blade diffusion factor, D	Loss coefficient, $\overline{\omega}$	Relative change in flow angle, $\Delta\beta'$
		Inlet	Outlet						
1R	0	3.250	3.087	0.108	0.133	0.655	0.2635	0.125	3.2
	2	2.964	2.844	↓	↓	.740	.2622	.100	6.0
	4	2.647	2.626			.809	.2496	.084	8.0
	6	2.287	2.411			.856	.2309	.080	9.8
	8	1.859	2.189			.899	.1871	.080	11.6
	10	1.296	1.954			.940	.0568	.090	12.6
2R	0	3.087	3.087	0.155	0.227	0.896	0.4171	0.079	2.3
	2	2.890	2.864	.181	↓	.933	.4356	.055	9.4
	4	2.705	2.700	.196		.948	.4423	.049	14.6
	6	2.520	2.550	.205		.956	.4511	.048	19.0
	8	2.329	2.404	.212		.960	.4564	.052	23.8
	10	2.130	2.258	.220		.963	.4498	.060	29.4
1S	0	3.087	3.087	0.128	-----	-----	0.5884	0.107	41.8
	2	2.864	2.950	.198	-----	-----	.5757	.096	28.5
	4	2.700	2.800	.237	-----	-----	.5681	.088	20.7
	6	2.550	2.635	.259	-----	-----	.5613	.080	16.0
	8	2.404	2.456	.277	-----	-----	.5520	.074	12.3
	10	2.258	2.258	.293	-----	-----	.5403	.067	9.7
3R	0	3.087	3.087	0.216	0.340	0.887	0.5573	0.113	9.9
	2	2.864	2.940	↓	↓	.914	.5692	.082	12.9
	4	2.700	2.785			.933	.6160	.063	17.9
	6	2.550	2.622			.949	.6822	.053	26.3
	8	2.404	2.447			.962	.7532	.051	41.3
	10	2.258	2.258			.972	.7853	.070	66.0

(1) Radially constant head rise

(2) Radially constant axial velocity

Satisfying the aforementioned conditions means that a symmetrical velocity diagram can be attained across only one blade element. In this design, the symmetrical velocity diagram was located at the mean blade element. The blade diffusion factor was limited to a value of approximately 0.55 at the tip but no limiting values were applied to other blade elements. The blade loading over the complete blade span was higher than that used in current practice. The selected radial distribution of loss coefficient was based on preliminary performance data from similar blade rows but with lighter loading. Using the previous conditions together with the definitions of a symmetrical velocity diagram results in the following velocity diagram calculations:

(1) At the blade mean streamline, a symmetrical velocity diagram is computed (see ref. 2 for discussion of symmetrical velocity diagram) based on an assumed blade diffusion factor. From the assumed loss coefficient, a head rise is calculated for application at all elements.

(2) The radial equilibrium equation (eq. (B5c)) is used to calculate inlet values of tangential velocity at all other radii.

Substitution of aforementioned design conditions ($\partial \Delta H/\partial r = 0$, $\partial V_z/\partial r = 0$, and $\overline{\omega}$ = known value) into equation (B5c) leaves rotor inlet (stator outlet) tangential velocity as the only unknown if blade element flow is assumed. Several iterations of the aforementioned procedure may be necessary before an acceptable value of blade tip diffusion factor is obtained. Iterations are also generally necessary in steps (1) and (2) before the calculated radial distribution of axial velocity at the stator outlet approaches the assumptions of axial velocity necessary in the computational procedures.

Throughout the design procedures used herein, the radial distributions of loss coefficient have been assumed. In more recent design procedures, the loss coefficient enters the calculations as some function of the blade loading and radial location of the blade element.

After the velocity diagram design data had been completed and applied in blade design calculations, a discrepancy in the second-stage rotor inlet velocity diagram was found. Across the stator, the assumed radial distribution of loss coefficient and the radial gradients of tangential velocity as established by the transition rotor outlet and second-stage rotor inlet flow conditions result in some mass flow shifts. Thus blade elements across the stator intercept inlet and outlet computational planes at different radii. The velocity diagram information computed for stator outlet (station 4 radii) was applied to the succeeding rotor inlet velocity diagram calculations at the stator inlet radii (station 3) rather than at the correct stator outlet values (station 4). This is reflected in the blade speeds presented for axial station 4 in table I (p. 6), which correlate with the radii at axial station 3 rather than 4. Subsequent tables of design values also show differences in the location of the streamlines leaving the stator outlet and entering the succeeding rotor. This results in maximum errors of 0.9° in relative flow angle and 5 feet per second in relative velocity, which occur at approximately the blade midspan. Because fabrication of the pump was nearly complete and the degree of error was small, it was not deemed necessary to correct these small discontinuities in streamline paths.

Blade Design

Blade shape. - Originally the inducer utilized a circular arc meanline with constant thickness from inlet to outlet along a given radius. The blade thickness varied linearly

with radius, increasing toward the hub. The circular arc meanlines were assumed to lie on conical surfaces intersecting the blade inlet and outlet computational planes at radii dividing these planes into equal flow areas, that is, blade element surfaces.

Before the inducer was built, some unpublished data were obtained on a similar inducer indicating that the performance of this inducer could be improved by revising the axial distribution of flow area to increase the passage area in the inlet portions of the blade row. This modification was expedited by adding a helical blade section to the leading edge of the inducer rotor. The helical portion extended an axial distance of 0.8 inch upstream of the inducer leading edge and had a constant passage area. At the blade tip (r = 3.25 in.) the helix angle matched the rotor blade inlet angle. At other radii some degree of fairing from the helical portion to the initial rotor design was required.

All other blade rows employed double circular arc blades. In all radial locations the double circular arcs lay along the assumed blade element, or streamline, surfaces.

Significant blade design parameters for six blade elements are presented in table III (p. 10).

Incidence and deviation angles. - For this design, selected incidence angles were based on some limited data from helical inducers and a double circular arc rotor.

Deviation angles of all the double circular arc blades rows were computed from the deviation angle rule of reference 5, which is defined as

$$\delta = m\varphi^{o}\sqrt{\frac{1}{\sigma}} \tag{3}$$

where m for circular arc cambered airfoils is given as a function of blade setting angle up to a maximum value of 60^{o}. Because the blade shape and range of inlet blade angles of the inducer were very different from those from which the design rule was formulated, the rule was not applied; deviation angles equal to one-fourth of the required turning angle were assigned. The latter values compare favorably with values computed from equation (3) if m is extrapolated to the inducer blade setting angles. It also can be noted from table III that the setting angles of a number of blade elements with double circular arc profiles were somewhat greater than the maximum values covered in the formulation of the rule and extrapolation was necessary.

Blade coordinates. - In the design procedures discussed thus far, each blade element has been assumed to lie on a conical surface intersecting the blade row inlet and outlet computational stations at points of equal weight flows. The complete blade is formed by stacking the blade elements on a radial line passing through the center of gravity of the individual sections. Cylindrical coordinates of the blade pressure and suction surfaces are obtained from a high-speed computer program.

For fabrication purposes, it is desirable to provide blade surface coordinates along

TABLE III. - BLADE DESIGN PARAMETERS

Blade row	Streamline number	Radius, r, in.		Incidence angle, i, deg	Deviation angle, δ, deg	Blade solidity, σ	Blade setting angle, γ, deg	Blade camber angle, φ^{o}, deg	Blade chord, c, in.	Maximum blade thickness, t_{max}, in. (a)	Entrance blade angle, κ_e, deg	Outlet blade angle, κ_o, deg	Number of blades
		Inlet	Outlet										
1R	0	3.250	3.087	3.0	0.8	3.65	----	1.0	----	0.060	80.9	79.9	3
	2	2.964	2.844	3.3	1.5	3.17	----	4.2	----	↓	80.0	75.8	↓
	4	2.647	2.626	3.6	2.0	2.95	----	6.4	----		78.9	72.5	
	6	2.287	2.411	4.2	2.5	2.82	----	8.1	----		77.2	69.1	
	8	1.859	2.189	5.0	2.9	2.71	----	9.5	----		74.4	64.9	
	10	1.296	1.954	6.9	3.1	2.62	----	8.9	----	.090	68.1	59.2	
2R[b]	0	3.087	3.087	2.0	0.5	1.47	76.1	0.9	1.50	0.075	----	----	19
	2	2.890	2.864	2.6	3.0	1.58	68.2	9.8	↓	↓	----	----	↓
	4	2.705	2.700	3.2	4.4	1.68	62.3	15.8			----	----	
	6	2.520	2.550	3.8	5.4	1.79	56.9	20.6			----	----	
	8	2.329	2.404	4.4	6.2	1.92	51.0	25.6			----	----	
	10	2.130	2.258	5.0	6.6	2.07	43.9	31.0		.120	----	----	
1S[b]	0	3.087	3.087	0	13.6	1.62	45.9	55.4	1.50	0.120	----	----	21
	2	2.864	2.950	↓	9.0	1.73	46.7	37.6	↓	↓	----	----	↓
	4	2.700	2.800		6.5	1.82	48.0	27.2			----	----	
	6	2.550	2.635		4.9	1.93	49.7	20.8			----	----	
	8	2.404	2.456		3.7	2.06	51.5	15.9			----	----	
	10	2.258	2.258		2.8	2.22	52.9	12.5		.060	----	----	
3R[b]	0	3.087	3.087	0	4.7	1.53	66.5	14.6	1.75	0.070	----	----	17
	2	2.864	2.940	↓	5.4	1.63	63.5	18.3	↓	↓	----	----	↓
	4	2.700	2.785		6.7	1.73	59.2	24.6			----	----	
	6	2.550	2.622		8.7	1.83	52.5	35.1			----	----	
	8	2.404	2.447	.7	11.0	1.95	41.9	51.6			----	----	
	10	2.258	2.258	4.0	13.0	2.10	24.0	75.0		.140	----	----	

[a] Linear distributions in blade maximum thickness used.

[b] $r_{\ell e} = r_{te} = 0.010$ in.

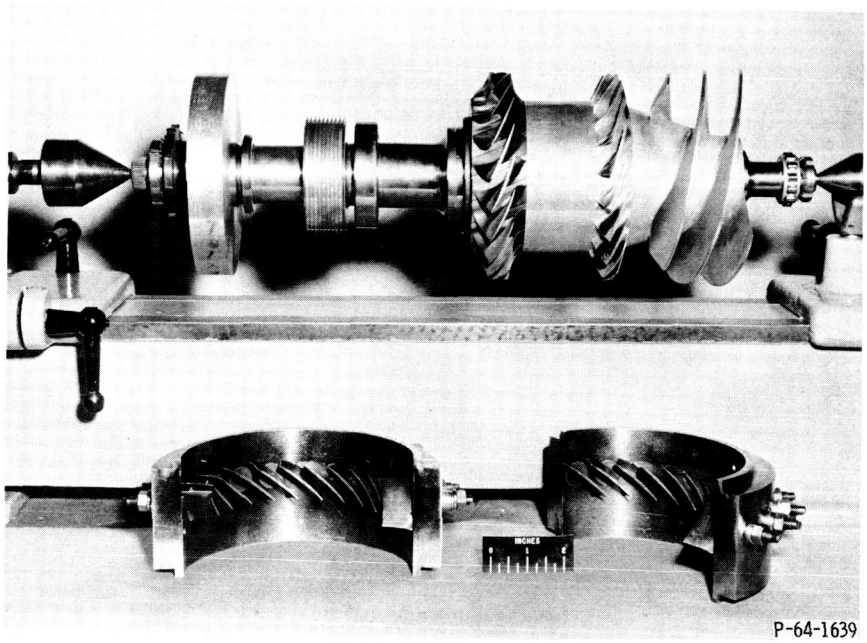

Figure 2. - Two-stage axial-flow pump.

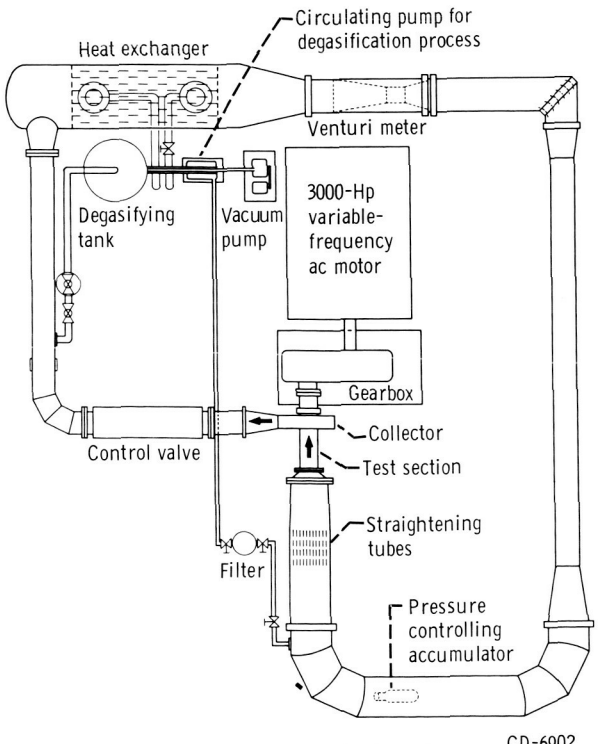

Figure 3. - Lewis water tunnel.

a constant radius plane. These are obtained using the blade surface coordinates from the computer program in a graphic procedure. A photograph of the pump is shown in figure 2.

APPARATUS AND PROCEDURE

Test Facility

The pump was tested in the Lewis water tunnel. The principal features of the water tunnel are shown in figure 3 and discussed in reference 6. Prior to the water tests, solid material larger than 5 microns was removed by the filtering system and the gas content was reduced to less than 1 part per million by weight with the auxiliary degasifying loop. During the tests, the gas content was maintained below 3 parts per million.

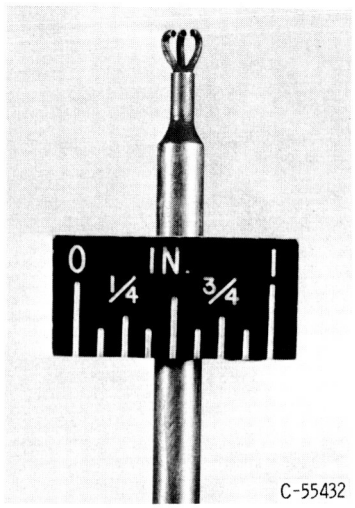

(a) Total pressure claw.

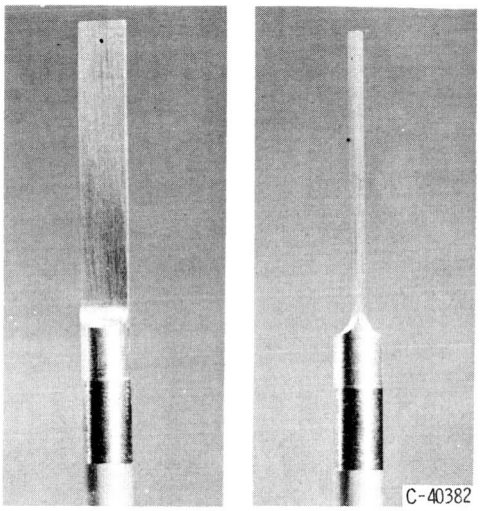

(b) Static pressure wedge.

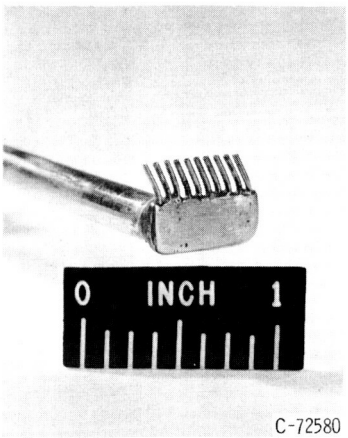

(c) Total pressure wake rake.

Figure 4. - Survey probes.

Instrumentation

The instrumentation used to obtain overall test loop conditions consisted of a venturi flowmeter, an electronic speed counter used in conjunction with a magnetic pickup, an automatic water temperature control and recorder, and a pressure transducer with the associated power and recording equipment to measure the loop pressure. The survey instruments (fig. 4) consisted of claw-type probes for measuring total head and angle behind rotating blade rows, a total head rake for measuring the wake behind the stators and wedge-type probes for measuring static head and angle. The measuring station locations are indicated in figure 1 (p. 3), which shows a meridional section of the pump. Each claw and wedge had null-balancing stream-direction-sensitive equipment that automatically alined the probe to the direction of flow. A head calibration factor for each wedge static probe was determined in a low-speed air tunnel at approximately the same Reynolds number used in water and applied to the static heads measured in the water tunnel. The inherent accuracies of measurement and recording devices were as follows:

Flow rate, Q, percent	$<\pm 1.0$
Rotative speed, N, percent	± 0.5
Differential heads, ΔH, percent	± 1.0
Flow angle, β, deg	± 0.5

This does not include possible errors due to circumferential variations in flow, unsteady flows, and other time or space gradients.

TABLE IV. - OPERATING CONDITIONS

Rotor tip speed, U_t, ft/sec	Net positive suction head, H_{sv}, ft
123	246
154	248
154	135
154	38
154	15

Procedure

Characteristic performance curves were obtained by operating the rotor at constant rotative speed and net positive suction head over a range of flow control valve settings. The data were taken by surveying total and static heads, and flow angles across the annulus at preprogramed radial positions located at approximately 10, 30, 50, 70, and 90 percent of design flow from the tip. The data presented were taken along characteristic curves for the conditions listed in table IV. The equations used to calculate selected performance parameters are presented in appendix B.

Data Reliability

Some measure of data reliability is available from weight flow checks, which are defined as the difference between the flow calculated from the survey data and the venturi flowmeter reading divided by the venturi reading. The weight flow checks are plotted against pump inlet flow coefficient in figure 5 for each of the five measuring stations. The circles in figure 5 (p. 14) represent data taken under noncavitating conditions and other symbols represent data taken under various degrees of cavitation.

The noncavitating data weight flow checks are within ±6 percent at measuring stations 1, 2, 3, and 5 with the exception of a few low-flow points where there is a flow reversal at the inlet of the inducer tip. At the measuring stations behind rotors, good blade-to-blade averages are obtained because the blades are moving with respect to the instrument. At station 4 behind the stators the weight flow differences run as high as 14 percent. At these measuring stations, the wakes are not moving with respect to the instruments so good average conditions are somewhat difficult to obtain. With the total pressure rake a good average value of total head is expected, but the blockage effect of the rake and particularly the angle measurements with the static probe present some problems. Although better data accuracy is desired, the accuracy obtained is as good as can be expected in small multistage machines with normal test procedure.

In general, the cavitating data weight flow checks are poorer than those calculated from the noncavitating data. One cause of this is probe cavitation, particularly on the static probe under some conditions. Observation of such cavitation through transparent casings over other rotors indicate that the total pressure readings are likely to be unaffected until the inlet pressure is lowered somewhat from that at which cavitation is first observed on the static probes. Thus, it is expected that the head rise measure-

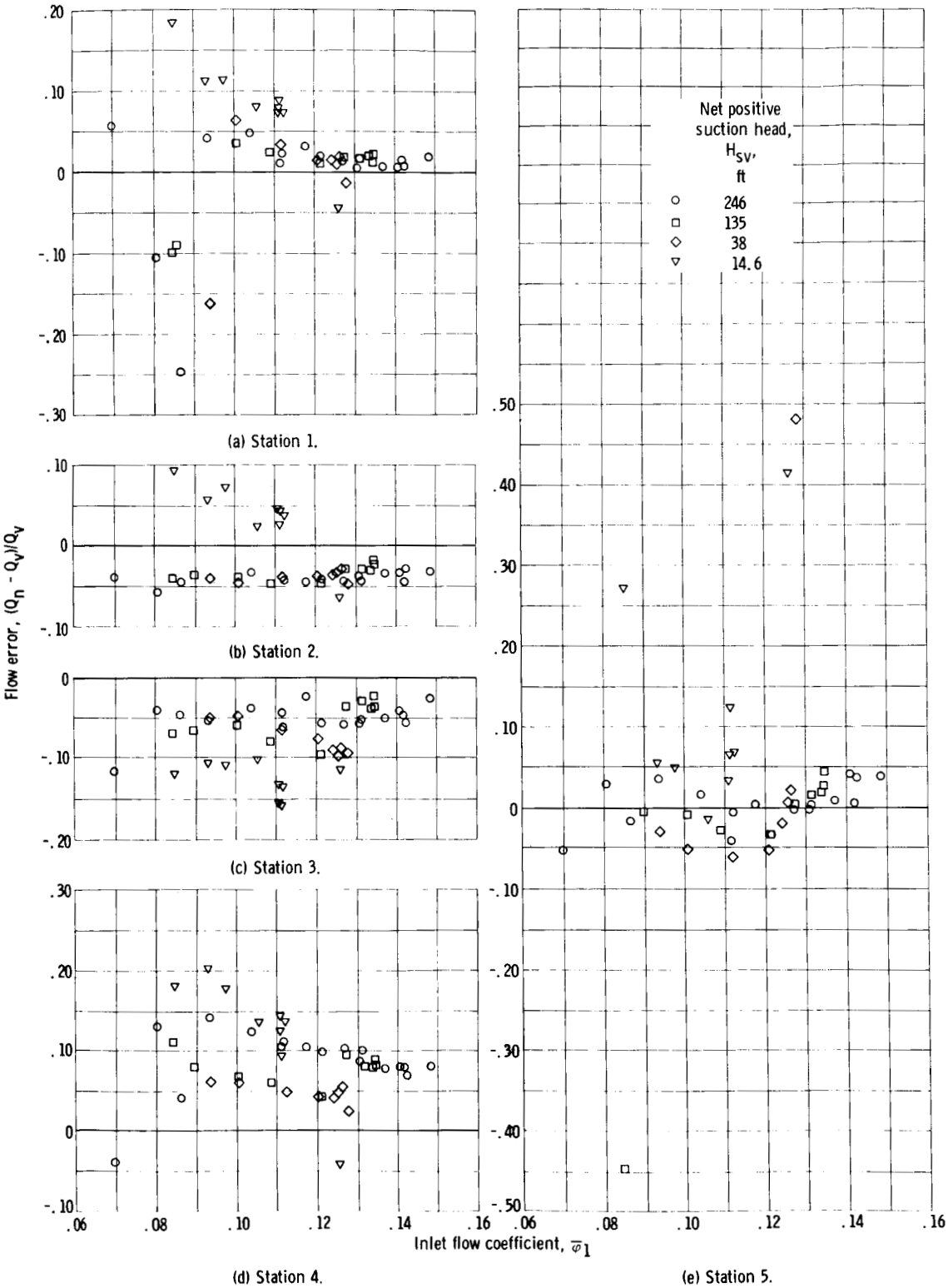

Figure 5. - Comparison of integrated weight flows with those measured with venturi meter.

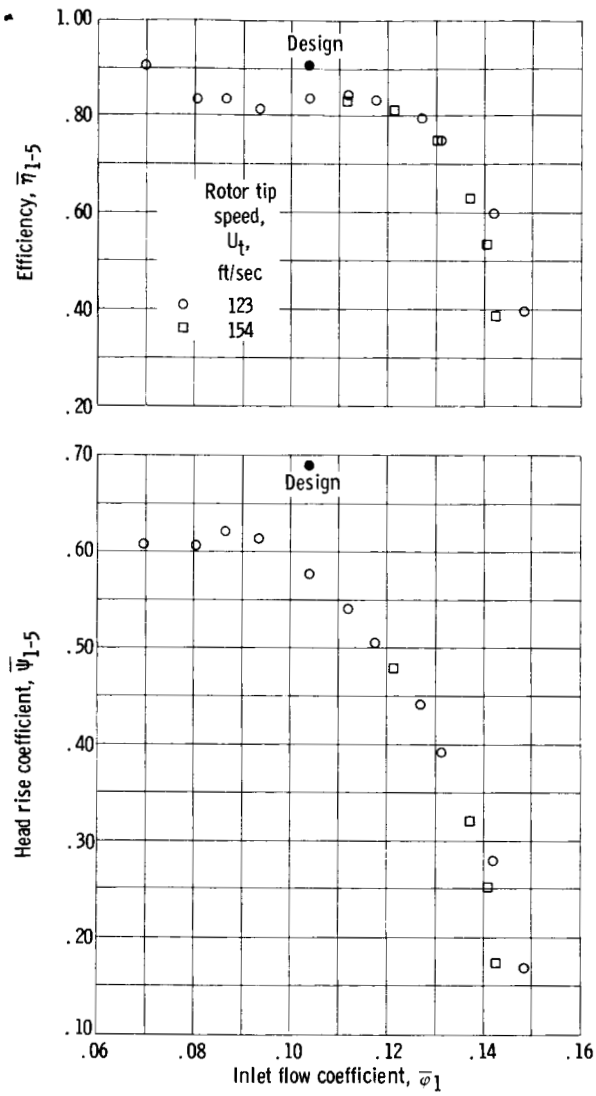

Figure 6. - Overall pump performance for noncavitating conditions. Net positive suction head, 246 feet.

ments under cavitating conditions are somewhat better than the weight flow data indicates. The accuracy of the velocity and efficiency calculations, however, can be expected to deteriorate with cavitation.

RESULTS AND DISCUSSION

The test results are presented as noncavitating and cavitating data. In this investigation, the noncavitating flow regime at a given wheel speed is defined as operation at inlet pressures above the pressure where a change in overall performance of the pump with a change in inlet pressure cannot be detected. Thus, the pump is not considered to have entered into the cavitating regime until cavitation is extensive enough to affect overall performance.

Noncavitating Performance

Overall pump performance. - The overall noncavitating performance is shown in figure 6 as head rise coefficient and efficiency plotted as functions of inlet flow coefficient. Design flow coefficient is considered to be 0. 104. This value is lowered from the ideal flow coefficient of 0. 108 to allow for hub and tip boundary layer blockage. The head rise coefficient and efficiency represent mass-averaged values, which were computed by the methods of appendix B, whereas the flow coefficient is an average value based on venturi-measured flows and inlet geometric area. The data shown were taken at two rotative speeds, 4330 and 5415 rpm, representing blade tip speeds of 123 and 154 feet per second, respectively. The data at 4330 rpm represent the noncavitating condition as defined earlier over the whole range of operation. Only the lower pressure (high flow) end of the characteristic curve at the design speed of 5415 rpm is shown. At low flow coefficients, the high inlet pressure combined with the head rise of the pump raised the exit pressure level to the point where the collector spread enough to open a

face seal from its mating surface. Even at this relatively high inlet pressure a falloff in performance due to cavitation is indicated at high flows, but the 5415-rpm data fair in with 4330-rpm data near the maximum flow point and are presumed to follow the noncavitating characteristic over the rest of the range. The 5415-rpm data are shown on the noncavitating curve because it is the design speed and it is used along with the 4330-rpm data as a reference condition for the lower inlet pressure data at 5415 rpm. At reduced inlet pressures, the collector pressure level was low enough so that the pump could be safely operated at the higher speed over the complete flow range.

The range of operation shown in figure 5 is limited on the high-flow end by the test loop losses when the flow control valve is completely open. As the flow was reduced, a recirculation at the inlet tip of the inducer began at a flow coefficient of 0.09 and increased in radial depth as the flow was decreased to 0.07 where radial surveys were terminated. The recirculation is probably due to a radial equilibrium requirement rather than blade stall because it was not accompanied by any appreciable increase in rig vibration. Since the presence of a recirculating flow region of some magnitude has the potential of triggering instabilities in some systems, however, the point of initiation of recirculation ($\bar{\varphi} = 0.09$) was selected as the criterion for the limit of the stable operating range. When recirculation at a measuring station occurs, mass-averaged values of head coefficients and efficiencies are difficult to determine. Head coefficients and efficiencies are mass weighted on the blade row outlet axial velocity distribution, but difficulties are still encountered when a recirculation occurs at the inlet only, because the inlet probes measure work done on the fluid by the blade row in the recirculation region. In general, the head values obtained from mass averaging under such adverse conditions are quite close to the mid survey point head rise values but the mass-averaged values of efficiencies are doubtful. It is in this light that the mass-averaged values for a flow coefficient below 0.09 are presented. More information on the characteristic curve in the low-flow region will be presented in a later figure in which midpoint data to shutoff flow is shown.

In comparing the data of figure 6 with design, it is apparent that the design head rise and efficiency were not attained. Not only was the efficiency low but the energy addition was not achieved since the percentage deficiency in head rise is somewhat larger than that indicated by the decrement in efficiency. Discussion of this is included in the blade-row performance section. Another point of interest is the location of design flow on the characteristic curve with respect to efficiency and range. Since the efficiency curve is relatively flat in the region of design flow, the design point could be moved to a slightly higher flow coefficient without a sacrifice in efficiency if it were desirable to have additional flow margin from design to the low flow limit of the stable operating range.

Blade-row performance. - The blade-row performance is presented in figure 7 by plotting cumulative head rise through the blade rows and efficiencies of the individual rotating blade rows against pump inlet flow coefficient. At design flow, the inducer

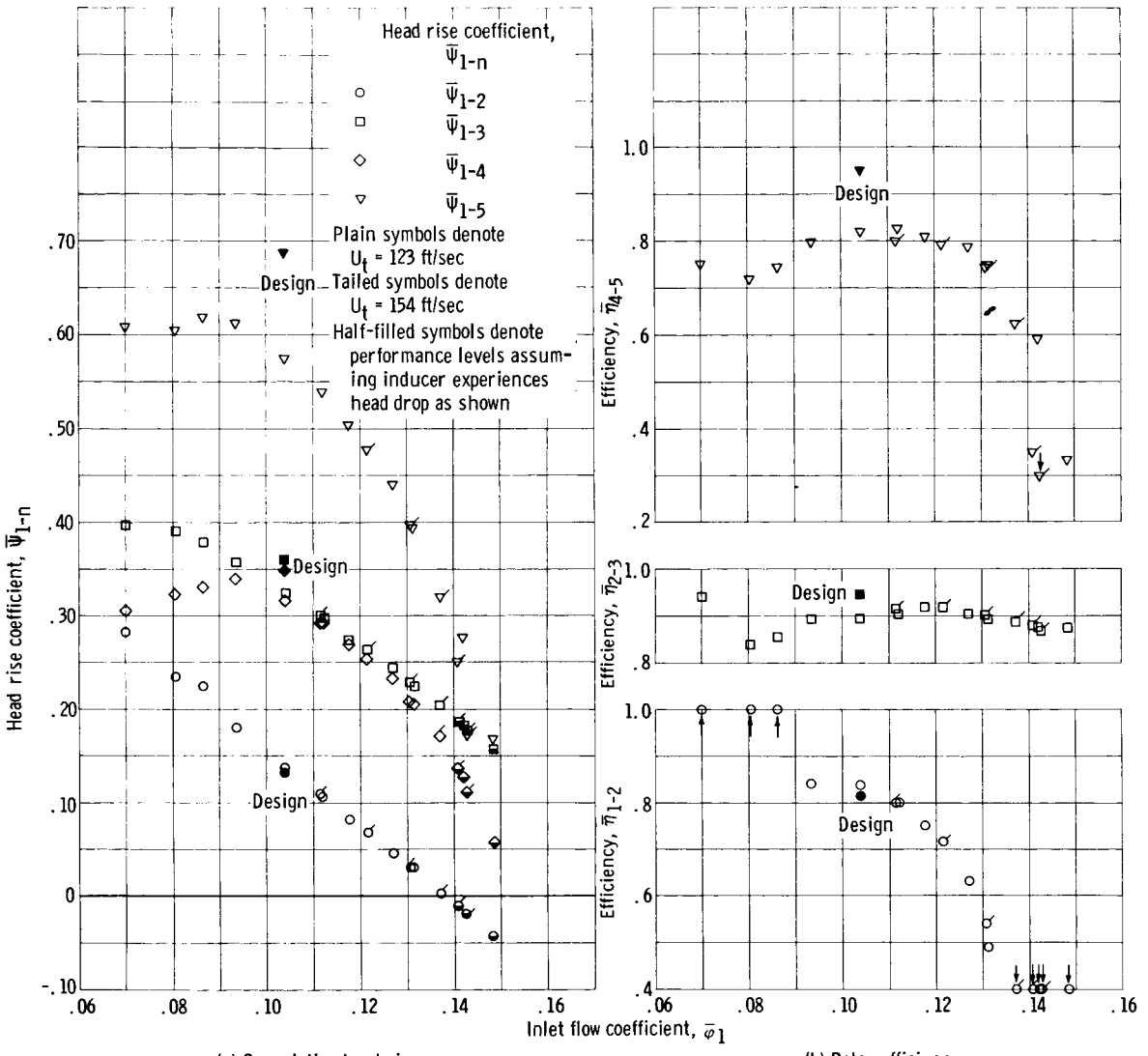

(a) Cumulative head rise.

(b) Rotor efficiency.

Figure 7. - Noncavitating performance. Net positive suction head, 246 feet.

achieved its design point and the stator losses were low; however, the transition and second-stage rotors fell far short of the design goals. The head rise across the transition rotor was 0.828 of the design value, and the efficiency was 0.945 of the design value. From these figures, the energy addition is only 0.876 of the design value, which is the major reason the transition rotor failed to achieve design head rise. The second-stage rotor head rise was 0.760 of the design value, and the efficiency was 0.860 of the design value. Thus, the energy addition was 0.883 of the design value, and hence, the energy addition and efficiency defects are about equally responsible for the head deficiency of this rotor.

From overall data, it is difficult to clearly resolve the causes of the deficiencies indicated above; however, some general observations are made. In regard to the transi-

tion rotor, it is suspected that the energy addition was not achieved because the deviation angles were larger than those anticipated in the design. It appears unlikely that flow separation on blade surfaces was the major cause since the blade loading was not especially high and the efficiency did not decrease as significantly as the energy addition. A more likely reason is associated with the fact that, as was noted previously in the design section, blade setting angles of a number of blade elements (in tip region) were larger than the values used to formulate the deviation angle prediction rule used in the design.

Across the second stage rotor with its high design blade loading, the significantly lower than design measured efficiency indicates the existence of thickened blade surface boundary layers or possibly some flow separation. Attendant effects would be to increase deviation angles. In addition, the blade setting angles for blade elements in the tip region required some extrapolation of the deviation angle design rule. Thus, although it is believed that the second-stage rotor did not achieve the design energy addition because it did not produce the desired fluid turning, the extent to which the deficit should be attributed to flow separation and extrapolation of the design deviation angle rule could not be further evaluated.

The blade-row characteristics in figure 7 show how the distribution of work between rotors changes with flow coefficient. At high flows the transition rotor does practically all the work and the inducer is turbining. A zero inducer head rise was measured at flow coefficients greater than 0.14 because the instrumentation was not set up to measure pressure drop. Since the transition rotor head rise and stator head drop are measured as differentials and added to the inducer head rise, the head levels in these regions are shown by the half-filled symbols in the figure. These were determined by assuming the inducer retains the same slope characteristic as it turbines. The stator losses in this region are several times the losses at design flow, and the second-stage rotor head rise barely compensates for these stator losses. As the flow is reduced, the inducer and second-stage rotor rapidly pick up large percentages of total pump work, while the transition rotor head coefficient changes very little. With no stator between the inducer and the transition rotor, the inlet relative fluid angle, and hence, incidence angle of the transition rotor changes very little with flow. Thus, the fluid turning and energy addition also change very little over the range of operation.

At the low flows ($\varphi < 0.09$) the inducer develops a recirculation at the inlet tip. As mentioned earlier, mass-averaged values are difficult to determine in a meaningful way under such conditions. In general, head distributions do not vary widely from hub to tip, so the method of averaging or flow reversals do not greatly affect the value attained. The value of efficiency, however, is quite sensitive to the axial velocity distribution and averaging method because the energy addition changes a great deal radially. No further effort was made to determine efficiencies of points where recirculation occurs, since, for the most part, the recirculation is inefficient and operation under such conditions is

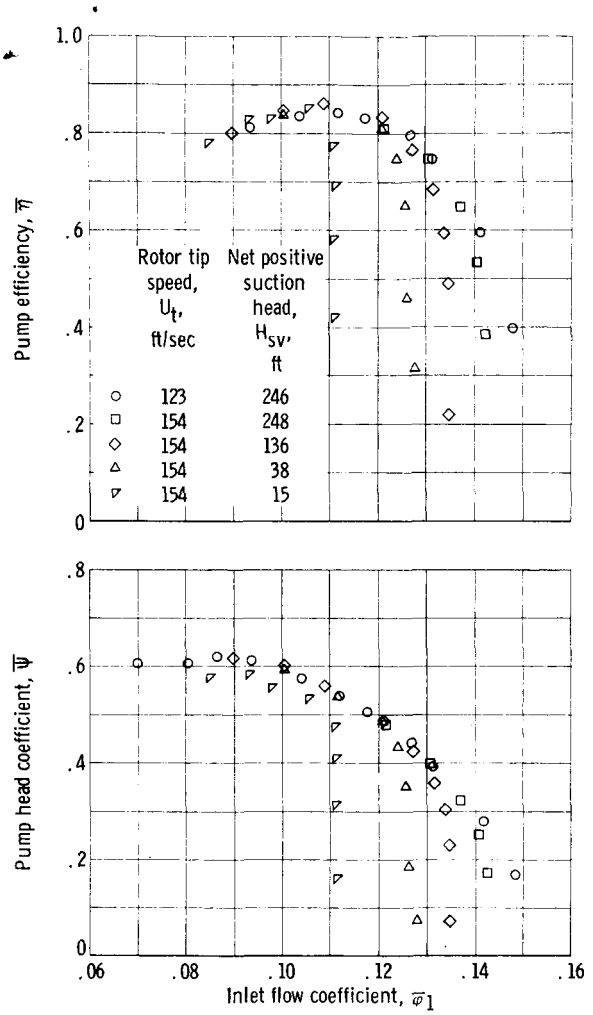

Figure 8. - Overall performance of axial-flow pump under cavitating conditions.

to be avoided as much as possible. In this low-flow region the other rotor efficiencies are on the decline but not because of recirculations. The stator losses increase rapidly as the stator incidence angles are increased far above design values.

Cavitating Performance

Overall pump performance. - The overall pump performance map for a range of net positive suction heads is shown in figure 8 as plots of head coefficient and efficiency against flow coefficient. Cavitation affects performance on the high-flow end of the characteristic at relatively high net positive suction heads. In fact, there is a slight head decrease at an H_{sv} of 248 feet when the rotor tip speed is 154 feet per second. This corresponds to a suction specific speed of approximately 3800. As the net positive suction head is reduced, the head and efficiency dropoffs become greater and the maximum flow becomes less. In each case, however, until an H_{sv} of 15 feet is approached, the characteristic remains unaffected for design and lower flows. At an H_{sv} of 15 feet (suction specific speed of approximately 27 000), the maximum flow rate is only slightly above the design flow, and the head, but apparently not the efficiency, has begun to fall at design and lower flows. The performance obtained indicates that a suitable operating suction specific speed ought to be a little lower than 27 000.

At maximum flow with an H_{sv} of 15 feet, the characteristic curve for the pump is practically vertical (no measurable change in flow) for head rise coefficients ranging from 0. 17 to 0. 45. At the lowest head rise (open throttle operating point) visual observations made during operation with a transparent casing showed that the stators and second-stage rotor were cavitating more severely than the inducer. These blade rows were very likely operating in the cavitation breakdown region where small changes in inlet pressure result in significant changes in head rise. As the throttle was adjusted to increase back pressure, the head rise across the inducer and transition rotor increased

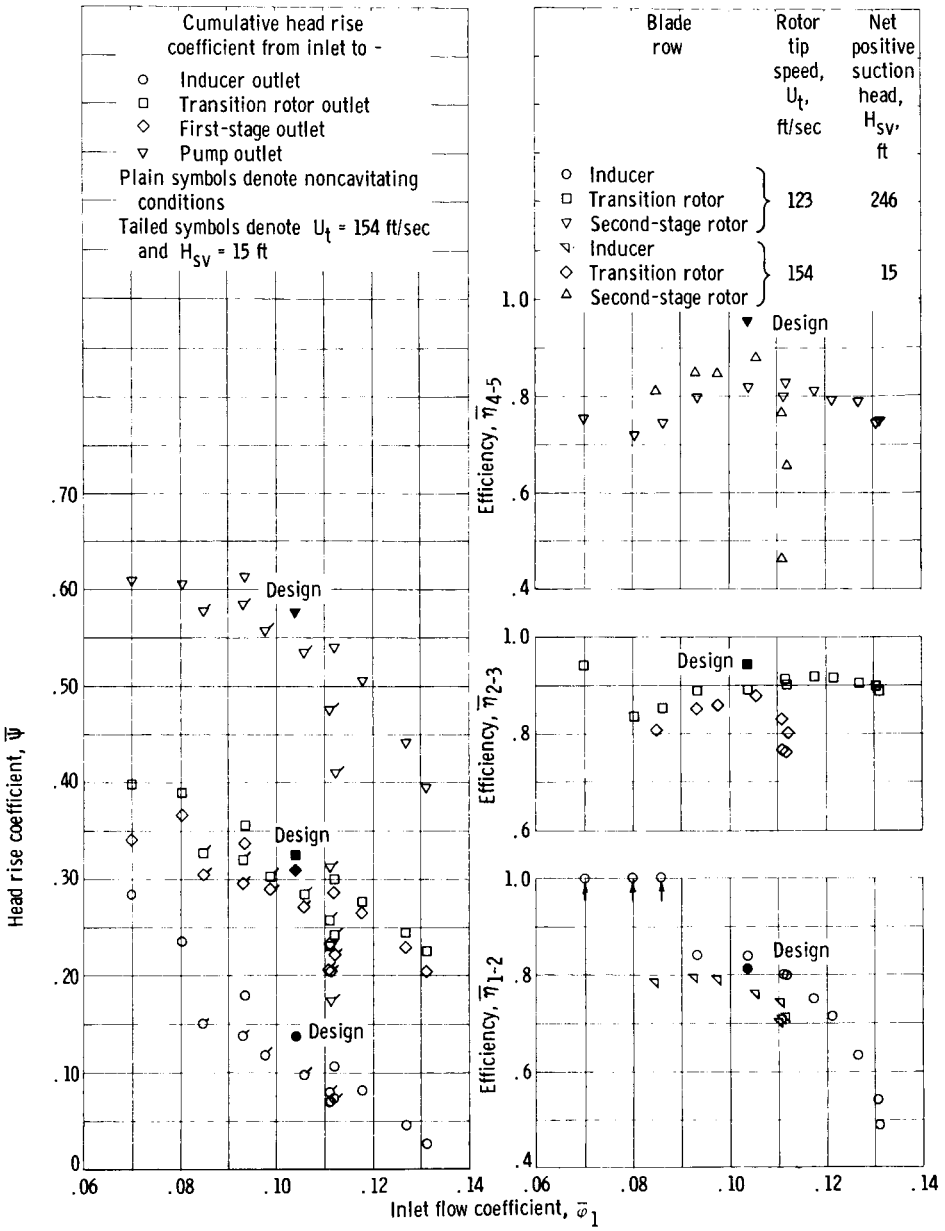

(a) Cumulative head rise. (b) Rotor efficiencies.

Figure 9. - Comparison of noncavitating and cavitating performance.

at only a moderate rate, but the effect was sufficient to give a rapid reduction in cavitation in the stator and second-stage rotor blade rows. The second-stage rotor head rise, and consequently the overall head rise, increased significantly without a measurable decrease in inlet flow coefficient. The mechanism described is also validated by visual observations. During operation at an overall head rise coefficient of 0.45, very little cavitation was observed in the stator or second-stage rotor blade passages.

Blade-row performance. - The cumulative head coefficients and individual rotor efficiencies for operation at an H_{sv} of 15 feet are compared with the noncavitating data in

figure 9. At this H_{SV} and design flow, a drop in head occurs only in the inducer as expected. All other cumulative head rises are displaced downward by approximately the amount of the inducer head defect. At design flow the inducer produces enough head to make the rest of the pump run virtually cavitation free. The rotor efficiencies at design flow, however, do not show entirely expected trends. The inducer efficiency drops 7 percentage points, and the transition rotor efficiency drops slightly. The second-stage rotor efficiency appears to rise about 5 percentage points and to compensate for the lower inducer efficiency to give essentially the same overall pump efficiency achieved under noncavitating conditions. This apparent rise in efficiency, however, is not believed to occur since the weight flow checks, especially those behind the stator under cavitating conditions, indicate data inconsistancies.

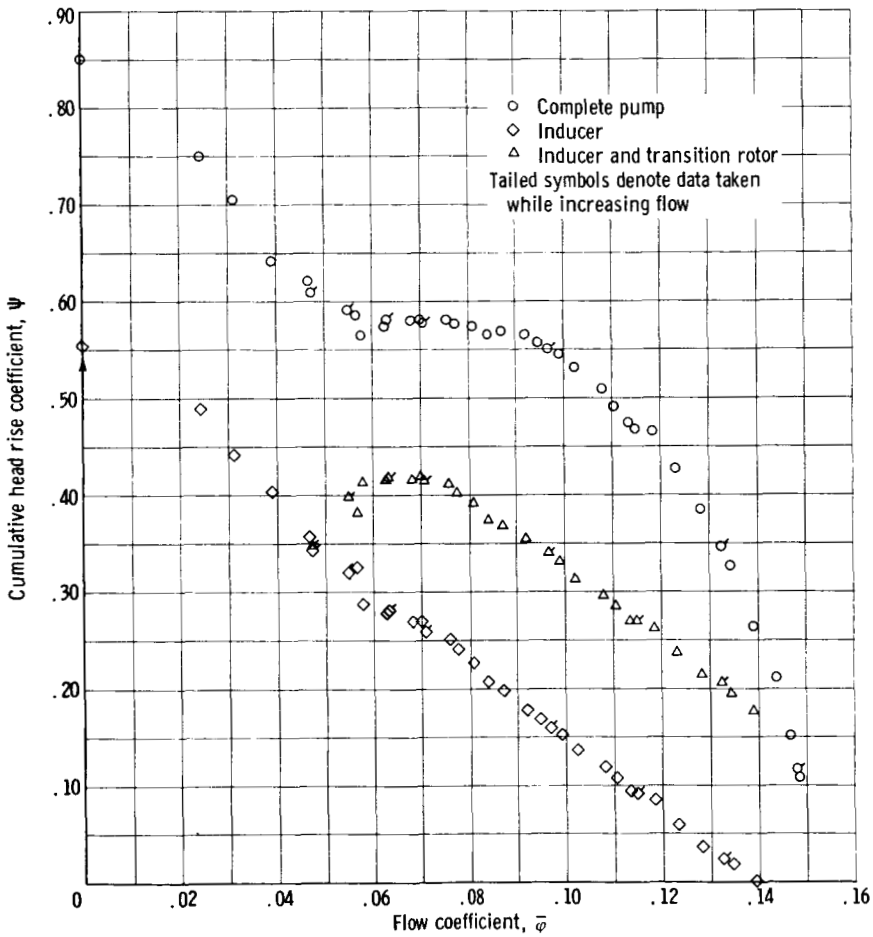

Figure 10. - Pump midpoint characteristic to zero flow under noncavitating conditions. Rotative speed, 4340 rpm.

Operation to Shutoff

Midpoint data were taken to determine the general pump characteristic to shutoff since this type of data can be useful for analysis of starting problems. For this data the total pressure probes were set at the 50-percent streamline for design conditions and left there for the run. The probes were alined to the flow with the automatic direction sensing equipment used in the surveys. The total pressure rake behind the stators was not used. The data making up this midpoint, noncavitating characteristic are presented in figure 10. Over the same flow range, midpoint data show very nearly the same characteristic as the mass-averaged data in figure 7 (p. 17). As flow is decreased into the stall region only a slight dip on head rise coefficient occurs before a rather steep negative slope develops to shutoff. Further, as flow is increased from shutoff, this inlet stage group unstalls smoothly along the same characteristic with no hysteresis.

Some complications arose in the determination of the work division between the inducer and transition rotors at low flows. Angle and head measurements between the inducer and transition rotor indicate that there is a backflow extending to the midstreamline position. Such a condition makes the inducer head rise appear to be very high and the transition rotor appear to turbine. Since the instrumentation was not set up to measure pressure drops across the transition rotor, the transition rotor head rise and the combined inducer and transition rotor data is missing for low flows. No attempt was made to determine the nature or extent of this recirculation by surveying the passage. The recirculation at the inducer inlet observed in the radial surveys did not extend to the midstreamline. Thus, the pump overall midpoint head rise, which was measured directly as a differential between outlet and inlet heads, was not affected by the aforementioned difficulties.

SUMMARY OF RESULTS

An inlet stage group for a high suction specific speed, multistage axial-flow pump was designed and tested in water. Analysis of the overall performance under both noncavitating and cavitating conditions and limited performance measurements with the pump operating in unstable flow regimes indicated the following principal results:

1. At design flow (average inlet flow coefficient $\overline{\varphi}_1 = 0.104$) under noncavitating conditions, the pump performance was far below the design head and efficiency. The inducer and stator operated to design predictions but the transition rotor and second-stage rotor did not.

2. The blade-row characteristics show major redistribution of work between rotors with change in flow coefficient.

3. At design flow under cavitating conditions (suction specific speed of 27 000) the pump head rise had begun to fall from the noncavitating values but the efficiency remained virtually unchanged. The drop in head occurred in the inducer.

4. At low net positive suction heads the pump characteristic on the high-flow side becomes almost vertical. At the low-head portion of the characteristic, the stators and second-stage rotor cavitate more severely than the inducer.

5. Noncavitating midpoint performance data in the very low-flow range show that the pump head rise has little dropoff in the stall flow range.

Lewis Research Center,
National Aeronautics and Space Administration,
Cleveland, Ohio, March 11, 1965.

APPENDIX A

SYMBOLS

c	blade chord, in.
D	blade diffusion factor, eq. (B3)
g	acceleration due to gravity, 32.17 ft/sec^2
H	total head, ft
ΔH	blade-element head rise, ft
H_{sv}	net positive suction head, $H_e - h_v$, ft
h	static head, ft
h_v	vapor pressure, ft
i	incidence angle (angle between inlet flow direction and tangent to blade mean camber line at leading edge) deg
k	cavitation number, eq. (B12a)
N	rotative speed, rpm
Q	flow rate, gal/min
r	radius, ft
t	blade thickness, in.
U	rotor tangential velocity, ft/sec
V	absolute velocity, ft/sec
β	flow angle with respect to axial direction, deg
$\Delta\beta$	change in flow angle
γ	blade setting angle (angle between blade chord and axial direction), deg
δ	deviation angle (angle between outlet flow direction and tangent to blade mean line at trailing edge), deg
η	rotor efficiency, percent
κ	blade angle (angle between tangent to blade mean camber line and axial direction), deg
σ	blade solidity (ratio of blade chord to blade tangential spacing)
φ	flow coefficient, $V_z/(U_t)_e$
φ^o	blade camber angle, deg
ψ	rotor head rise coefficient, $g\,\Delta H/(U_t^2)_o$
$\overline{\omega}$	loss coefficient, eq. (B4a)

Subscripts:

e	entrance to blade row
h	hub
i	ideal
ℓe	blade leading edge
max	maximum
n	axial station, see fig. 1
o	outlet of blade row
t	tip
te	blade trailing edge
v	measured with venturi meter
z	axial component

θ tangential component

1 inducer inlet measuring station

2 inducer outlet and transition rotor inlet measuring station

3 transition rotor outlet and stator inlet measuring station

4 stator outlet and second-stage rotor inlet measuring station

5 second-stage rotor outlet measuring station

Superscripts:

$-$ averaged quantity

$'$ relative

APPENDIX B

EQUATIONS

Blade Element Equations

Ideal head rise (energy input):

$$\Delta H_i = \frac{U_o V_{\theta,o} - U_e V_{\theta,e}}{g} = \Delta H + \overline{\omega}\frac{(V_e')^2}{2g} \qquad \text{(B1)}$$

Efficiency:

$$\eta = \frac{\Delta H}{\Delta H_i} \qquad \text{(B2)}$$

Diffusion factor:

$$D = 1 - \frac{V_o'}{V_e'} + \frac{r_o V_{\theta,o} - r_e V_{\theta,e}}{2\sigma V_e' \overline{r}} = 1 - \frac{V_o'}{V_e'} + \frac{r_o V_{\theta,o} - r_e V_{\theta,e}}{(r_o + r_e)\sigma V_e'} \qquad \text{(B3)}$$

Total head loss coefficient:

$$\overline{\omega} = \frac{H_{o,i}' - H_o'}{\frac{(V_e')^2}{2g}} \qquad \text{(B4a)}$$

When applied to a rotating blade row, equation (B4a) becomes

$$\overline{\omega} = \frac{\Delta H_i - \Delta H}{\frac{(V_e')^2}{2g}} \qquad \text{(B4b)}$$

When applied to a stationary blade row, equation (B4a) becomes

$$\overline{\omega} = \frac{H_e - H_o}{\frac{V_e^2}{2g}} \tag{B4c}$$

In both design and analysis procedures, radial equilibrium was assumed to be achieved at each measuring station when the radial pressure gradient balanced the centrifugal acceleration of the fluid due to its whirling motion, or

$$\frac{\partial h}{\partial r} = \frac{V_\theta^2}{gr} \tag{B5a}$$

Since

$$h = H - \frac{V^2}{2g} = H - \frac{V_r^2}{2g} - \frac{V_\theta^2}{2g} - \frac{V_z^2}{2g}$$

equation (B5a) can be written in terms of total head and velocities. With the radial component of velocity neglected, equation (B5a) becomes

$$\frac{\partial V_z^2}{\partial r} = 2g \frac{\partial H}{\partial r} - \frac{\partial V_\theta^2}{\partial r} - 2 \frac{V_\theta^2}{r} \tag{B5b}$$

For some applications, it is desirable to relate the radial distribution of outlet flow conditions to the inlet flow conditions and the change occurring across the blade row. By using the following relations:

$$H_o = H_e + \Delta H$$

$$\Delta H = \Delta H_i - \overline{\omega} \frac{(V_e')^2}{2g} = \frac{U_o V_{\theta,o} - U_e V_{\theta,e}}{g} - \overline{\omega} \frac{(V_e')^2}{2g}$$

$$= \frac{1}{g}\left(U_o^2 - U_o V_{z,o} \tan \beta_o' - U_e^2 + U_e V_{z,e} \tan \beta_e'\right) - \omega \frac{(V_e')^2}{2g}$$

equation (B5a) can be written with a large variety of inputs. In the design procedure

used herein, equation (B5a) was written with ΔH, $\overline{\omega}$, and inlet velocity diagrams as the known inputs. Hence, equation (B5a) takes the form

$$\frac{\partial V_{z,o}^2}{\partial r_o} = 2g\frac{\partial H_e}{\partial r_o} + 2g\frac{\partial(\Delta H)}{\partial r_o} - \frac{\partial}{\partial r_o}\left[\frac{g\,\Delta H + \omega\frac{(V_e')^2}{2} + U_e V_{\theta,e}}{U_o}\right]^2 - \frac{2}{r_o}\left[\frac{g\,\Delta H + \overline{\omega}\frac{(V_e')^2}{2} + U_e V_{\theta,e}}{U_o}\right]^2 \tag{B5c}$$

Later design procedures used ΔH_i as input and calculate a blade diffusion factor and an associated $\overline{\omega}$.

Averaging Methods to Obtain Overall Parameters

Allowance is made for the hub and casing boundary layers in the two end terms of each of the following summations:

Mass-averaged head rise:

$$\overline{\Delta H} = \overline{H}_o - \overline{H}_e = \frac{\sum_{r_h}^{r_t} r_o V_{z,o} H_o \Delta r_o}{\sum_{r_h}^{r_t} r_o V_{z,o} \Delta r_o} - \frac{\sum_{r_h}^{r_t} r_e V_{z,e} H_e \Delta r_e}{\sum_{r_h}^{r_t} r_e V_{z,e} \Delta r_e} \tag{B6}$$

Mass-averaged energy addition (ideal head rise):

$$\overline{\Delta H_i} = \frac{\overline{U_o}\,\overline{V_{\theta,o}}}{g} - \frac{\overline{U_e}\,\overline{V_{\theta,e}}}{g} = \frac{\frac{1}{g}\sum_{r_h}^{r_t} r_o V_{z,o} U_o V_{\theta,o} \Delta r_o}{\sum_{r_h}^{r_t} r_o V_{z,o} \Delta r_o} - \frac{\frac{1}{g}\sum_{r_h}^{r_t} r_e V_{z,e} U_e V_{\theta,e} \Delta r_e}{\sum_{r_h}^{r_t} r_e V_{z,e} \Delta r_e} \tag{B7}$$

Mass-averaged efficiency:

$$\overline{\eta} = \frac{\overline{\Delta H}}{\overline{\Delta H_i}} \tag{B8}$$

Mass-averaged head coefficient:

$$\overline{\psi} = \frac{g\,\overline{\Delta H}}{U_{t,o}^2} \tag{B9}$$

Average flow coefficient (no boundary layer correction):

$$\overline{\varphi}_1 = \frac{Q_v}{448.8\,\pi(r_t^2 - r_h^2)U_{t,1}} \tag{B10}$$

Cavitation number:

A local cavitation number is defined by

$$k = \frac{h_e - h_v}{\frac{(V_e')^2}{2g}} = \frac{2gH_{sv}}{(V_e')^2} - \frac{V_e^2}{(V_e')^2} \tag{B12a}$$

For application to the inducer where the inlet total head is constant radially and the inlet flow has no whirl component ($V_{\theta,e} = 0$) an average or blade cavitation number of the following form is used:

$$\overline{k} = \frac{2gH_{sv}}{U_{t,e}^2(1 + \overline{\varphi}_e^2)} - \frac{\overline{\varphi}_e^2}{1 + \overline{\varphi}_e^2} \tag{B12b}$$

REFERENCES

1. Ross, C. C.; and Banerian, Gordon: Some Aspects of High-Suction Specific-Speed Pump Inducers. Trans. ASME vol. 78, no. 8, Nov. 1956, pp. 1715-1721.

2. Wu, Chung-Hua; and Wolfenstein, Lincoln: Application of Radial-Equilibrium Condition to Axial-Flow Compressor and Turbine Design. NACA TN 1795, 1949.

3. Hatch, James E.; Giamati, Charles C.; and Jackson, Robert J.: Application of Radial-Equilibrium Condition to Axial-Flow Turbomachine Design Including Consideration of Change of Entropy with Radius Downstream of Blade Row. NACA RM E54A20, 1954.

4. Crouse, James E.; Soltis, Richard F.; and Montgomery, John C.: Investigation of the Performance of an Axial-Flow-Pump Stage Designed by the Blade-Element Theory - Blade-Element Data. NASA TN D-1109, 1961.

5. Carter, A. D. S.; and Hughes, Hazel P.: A Theoretical Investigation into the Effects of Profile Shape on the Performance of Airofoils in Cascade. Rept. No. R.&M. 2384, British A. R. C., 1946.

6. Crouse, James E.; Montgomery, John C.; and Soltis, Richard F.: Investigation of the Performance of an Axial-Flow-Pump Stage Designed by the Blade-Element Theory - Design and Overall Performance. NASA TN D-591, 1961.